Available online at www.sciencedirect.com

Manufacturing Letters

Manufacturing Letters 35 (2023) 665-676

51st SME North American Manufacturing Research Conference (NAMRC 51, 2023)

Gas Bubble Coalescence in Laser Directed Energy Deposition of Irregular HDH Titanium Alloy Powder Feedstock

Marwan Haddad[a], Aslan Bafahm Alamdari[a], Karan Vinod Kankaria[b], Hui Wang[b],
Benjamin Gould[c], Sarah J. Wolff[a] *

[a]*Department of Mechanical and Aerospace Engineering, The Ohio State University, Columbus, OH 43055, USA*
[b]*Department of Industrial & Systems Engineering, Texas A&M University, College Station, TX 77843, USA*
[c]*Advanced Performance Materials, The Chemours Company, Wilmington, DE 19899, USA*

* Corresponding author. *E-mail address: wolff.357@osu.edu*

Abstract

In this study, the synchrotron X-ray imaging technique was used to investigate the coalescence of gas bubbles during laser directed energy deposition (L-DED) of irregular hydride-dehydride (HDH) titanium alloy particles onto a titanium alloy substrate. The objective is to better understand the coalescing mechanism of gas bubbles during the L-DED process of unique feedstock materials. The coalescence frequency of gas bubbles is the percentage of bubbles merging and is dependent on collision frequency and coalescence efficiency. Forces in the melt pool flow such as Marangoni forces, buoyancy force, vaporization pressure, and acoustic waves, along with the number of generated bubbles, were the major factors for increasing the collision frequency between bubbles. In addition, the random forest model determined that the diameter of the smaller bubble during collision was the most significant factor impacting the efficiency of coalescence, which was equal to 48% when the smaller diameter was larger than a threshold of 76 µm and 3.5% and when the diameter was smaller than 76 µm. The results also showed that 6.5% of the formed bubbles in the melt pool led to coalescence. Overall, this work can help mitigate pores, verify simulation models, and promote irregular or recycled powder feedstock as effective replacement to atomized feedstock.

Keywords: In situ monitoring; X-ray imaging; Laser directed energy deposition; Gas bubbles; Porosity; Coalescence; Irregular powders.

---

1. Introduction

Laser directed energy deposition (L-DED) is a metal additive manufacturing process in which metal powders are fed on top of a melt pool created by an energy source such as a laser beam on a substrate. The L-DED process allows the use of multiple types of materials during the print functionally graded parts or compositionally complex alloys [1, 2]. Additionally, L-DED has advantages compared to several types of conventional welding processes for restoration and remanufacturing applications. L-DED can reduce material and energy consumption during operation since the process has lower energy input, less distortion and warpage, higher cooling rates, and strong bonding between the deposited layers [2]. Therefore, L-DED has gained more recent attention from the remanufacturing industry than conventional manufacturing processes [1, 2, 3, 4, 5, 6].

However, L-DED still undergoes challenges that affect the repeatability of the process and quality of printed parts, such as low accuracy, rough surface finish, residual stress, and defects formation in printed parts [4, 7]. Defects, such as distortion, cracks, and porosity, affect the mechanical properties such as fatigue and tensile strength of the build in L-DED, and therefore are a bottleneck to qualification and certification [4,8]. Porosity can also lead to other forms of defects, such as hot cracking [9] and surface roughness from surface pores [10]. In addition, porosity studies can help in developing the requirements for qualification and certification of metal additive manufacturing for high precision industrial applications, including aerospace, automotive, biomedical, and energy industries [11].

Conventional literature discusses two broad categories of pores: (1) gas-entrapped pores, (2) lack of fusion pores. Pores are also classified as internal pores and surface pores and they vary in size and shape. For example, lack of fusion pores generally have irregular shapes and gas pores are mostly spherical, though there are many exceptions depending on the process parameters and process dynamics [10, 12, 13]. Several methods of in situ observations have already been conducted by researchers to study the fundamentals of pore formation mechanisms in L-DED. One method is using an in situ synchrotron X-ray imaging system to monitor the L-DED process. This in situ system captures images in real-time with high spatial and temporal resolutions to help understand the distinct types of dynamics leading to defect formation [1, 7, 12, 13, 14]. Wolff *et al.* investigated four types of internal pore formation mechanisms found in L-DED processes using irregular shaped hydride-dehydride (HDH) Ti-6Al-4V (Ti64) powder feedstock with ultra-fast X-ray imaging. These types included (1) pores due to feedstock powder characteristics; (2) pores produced by keyhole instability; (3) pores generated from the interaction between powder particles and melt pool; and (4) pores formed by the interaction between the inert carrier gas and the melt pool [1]. Furthermore, Wang *et al.* studied the internal pore mechanism during the L-DED process of spherical Ti64 powders using synchrotron X-ray imaging [14]. They showed that the main cause of porosity was the interaction between the spherical particles and the melt pool [14]. The interactions were described as: (1) the interaction between the front side of the melt pool and powder particles and (2) the interaction between different sides of a powder particle with the back side of the melt pool [14]. Lastly, Chen *et al.* examined lack of fusion pores in a L-DED process of titanium alloy Ti6Al-2Sn-4Zr-2Mo (Ti6242) powders on titanium Ti-6Al-2Sn-4Zr-6Mo (Ti6246) substrates [7]. From the X-ray images, they hypothesized that the cause for lack of fusion pores was the sintering of powders deposited on the track before and after the melt pool which was caused by the removal of the oxide layer from the surface of the powders at elevated temperatures [7].

Another method of capturing porosity formation in real-time is high speed imaging coupled with infrared (IR) imaging. This method was used by Zhang *et al.* to analyze surface pores during a L-DED process of a powder feedstock with a nominal composition of Ni–8Cr–6Al–6Co–5W in wt.% [4]. In their experiments, pores were created on the surface of the tracks caused by the solidification of gas bubbles generated from the entrapment of air. The movements of the gas bubbles on the liquid surface were dominated either by the combination of Marangoni flow, the impact of the powders and the carrier gas on the top surface of the melt pool, the motion of the boundary for single track layers or by melt pool geometry for multi-tracks layers [4].

As discussed above, previous work tackled the fundamentals of pore formation due to lack of fusion or gas-entrapped bubbles in the L-DED process. However, the analysis of gas bubbles dynamics before conversion into pores during solidification has not been examined for the L-DED process. Gas bubbles have different trajectories while moving in the melt pool and reside as pores in unpredictable locations in the final build. Gas bubbles also vary in size and can coalesce to form new bubbles, which either stay in or escape the melt pool. Furthermore, the number and size of the gas bubbles determine the porosity percentage of the final build. Consequently, to achieve better quality structures, understanding how gas bubbles behave and interact is important to develop better pore mitigation/elimination strategies and to develop/improve simulation techniques to attain better prediction of the different dynamics in the L-DED process for better quality printed parts.

There is increasing attention on studying irregular HDH metal powder feedstock and how they can affect the final build in LAM processes. These types of feedstocks can be a less expensive alternative to atomized feedstock [1] and can conform to the remanufacturing industry conditions with recycled powders during production [15]. For example, in an electron beam powder bed fusion process, Narra *et al.* used HDH Ti64 powders and examined the porosity and the microstructures of the samples, which exhibited good properties compared to samples fabricated using spherical powders [15]. Terrassa *et al.* reused 316L stainless steel powder in a L-DED process and indicated that the recycled powders increased the number of internal pores in the build, however the overall properties of the samples did not vary [16]. In addition, Xu *et al.* processed HDH titanium powders using ball milling to achieve near spherical shaped powders for a selective laser melting process, with the resulted samples exhibiting good mechanical properties [17].

The study's objective is to fill in the knowledge gaps of how bubbles, and therefore pores, form with HDH powder feedstock and how they evolve in the melt pool in real-time. Hence, this work quantifies the coalescence of gas bubbles during the deposition of irregular Ti64 powders on Ti64 substrates in a L-DED process. The analysis is focused on discovering the significant factors contributing to the frequency of bubble coalescence. Using an in situ high-speed X-ray imaging system, the investigation on the different phenomena that may influence the collision frequency inside of the melt pool was performed, along with a statistical approach to quantify the importance of the parameters that may be significant to bubble coalescence efficiency.

2. Bubble coalescence mechanism in L-DED

Coalescence of gas bubbles is a complex phenomenon since bubbles not only interact with the surrounding fluid, e.g., the liquid metal Ti64 in this study, but also with other bubbles [18]. Different factors may be involved in the collision and coalescence mechanisms of two bubbles. The coalescence frequency is the percentage of two parent bubbles coalescing, and it depends on the collision frequency and the coalescence efficiency [18]. The collision frequency is the frequency of two parent bubbles colliding with each other, and the efficiency of coalescence is the efficiency of bubbles coalescing after collision. Through the literature, empirical and physical models were applied to define and predict the mechanism of fluid particles in a multiphase flow [18]. The general form that defines the coalescence frequency can be written as follows:

$$\Gamma\left(d_1, d_2\right) = h\left(d_1, d_2\right)\lambda\left(d_1, d_2\right) \tag{1}$$

Where $\Gamma(d_1, d_2)$ represents the coalescence frequency, $h(d_1, d_2)$ is the collision frequency, $\lambda(d_1, d_2)$ denotes the coalescence efficiency, and d_1, d_2 are the diameters of each parent bubble [18].

Collision frequency might be related to distinct types of forces and flows in the melt pool. To determine the forces that contribute to collision, in situ X-ray imaging can be applied. For example, Leung *et al.* reported that the Marangoni flow promoted the collision and merge of bubbles created in the melt pool of an Invar 36 powders for a LPBF process [19, 20]. In the case of a L-DED process, studies were not conducted yet to determine the major forces acting on the bubbles' movements. However, based on the work done by Wang *et al.* an analogy can be made between the different forces affecting the movement of a particle during an alloying process in L-DED to show which are the forces that might affect the movement of bubbles [21]. Figure 1a illustrates different sections where each of these driving forces is dominant inside the melt pool. Section 1 (S1) is where the Marangoni forces are dominant as they drive particles from regions with lower surface tension to regions with higher surface tension. At section 2 and 3 (S2, S3), a hydraulic pressure at the boundary moves the flow downwards back to the keyhole. In section 4 (S4), resides a combination of the hydraulic pressure at the liquid-solid boundary and the buoyancy force in the center of the melt pool, which brings the flow downward first, then upward to the surface. Additionally, section 5 (S5) is where the Marangoni forces and the vaporization pressure direct the flow upward, which is in contrast with section 6 (S6) where the same forces drive the flow in the downward direction [21]. The physical equations of the driving forces in each section are found in the work done by Wang *et al.* [21]. Furthermore, Zhao *et al.,* added another mechanism in the flow when the process had a keyhole melting mode. They found that acoustic waves, generated from the instability of the keyhole tip, pushed the flow away from the vapor depression zone (keyhole) during their investigation of an L-PBF process [12]. Hence, another section (S7) was added to Fig. 1a where acoustic waves are the dominant driving mechanisms in the flow in the case of instability of the keyhole tip. The force from the acoustic wave can be interpreted as a microjet pressure in a liquid metal and approximated in Eq. (2), where p_{jet} is the impact pressure from the jet, ρ_m is the mass density of the liquid metal, C is the speed of sound in liquid and V_{jet} is the speed of the jet. Because the jet is generated from a conical tip, which is the keyhole tip, a multiplication factor greater than 1 is usually added [12].

$$p_{jet} = \frac{1}{2}\rho_m C V_{jet} \tag{2}$$

Three models were introduced to interpret the coalescence efficiency of two bubbles in a liquid flow in the literature [18]. The first model is the energy model, where the efficiency of two bubbles merging increases with higher collision energy. This type of model hypothesized that the collision generates an immediate coalescence of the two gas bubbles. The second model is the critical approach velocity model, which also stated that coalescence is also immediately after the collision if the velocity of the bubbles exceeds a critical velocity. The third and the most well-known is the film drainage model [18]. The principle of the model is that after the collision, the two bubbles are separated by a thin film caused by trapped liquid between them [18]. Depending on the forces acting on the bubbles, the thin liquid film drains out until reaching a critical thickness at which the film breaks down and the bubbles coalesce [18]. The contact time is the total duration of contact between the two bubbles before complete coalescence [18]. Figure 1b shows a schematic of the film drainage model, where two parent bubbles, with their respective diameters d_1 and d_2, collide with each other due to the existing forces in the flow. Then, the bubbles are separated with a liquid film, which is caused by the pressure gradient between the deformed interfaces, trapped between the two bubbles [18]. Finally, after the two bubbles are in contact with each other, the thin film collapses and the two bubbles merge into one daughter bubble.

3. Experimental setup and materials

A custom-made in situ/operando system for X-ray imaging experiments was designed to replicate a L-DED system. A full description of the setup can be found in [1, 14, 21]. The main components included a powder delivery system (with a single nozzle), argon gas cylinder, chamber system, laser scanning system (Ytterbium fiber laser, maximum laser power of 520 W, wavelength 1070 nm, and spot size 100 μm), and a substrate system [1, 14, 21]. The setup was installed at the 32-ID-B beamline at the Advance Photon Source (APS) located at the Argonne National Laboratory (ANL). Figure 1c shows different components of the in situ/operando experimental setup [1, 14, 21]. Figure 1d displays a schematic illustration inside of the chamber, showing a singular nozzle delivery system attached to a rotary stage with an inclination angle of 60° with the horizontal, and a substrate. The rotary stage controls the motion of the nozzle to fix the distance between the laser beam and the nozzle during printing to approximately 0.3 mm vertically [1, 14, 21]. Two experiments were conducted using one type of powder feedstock deposited on a Ti64 substrate placed between two glassy carbon plates. Both experiments had the same input parameters: laser power 208 W, scanning speed 0.1 m/s and scanning distance 1.4 mm. Irregular HDH titanium powder (Ametek Specialty Metal Products, Cypress, Texas, USA, now known as Reading

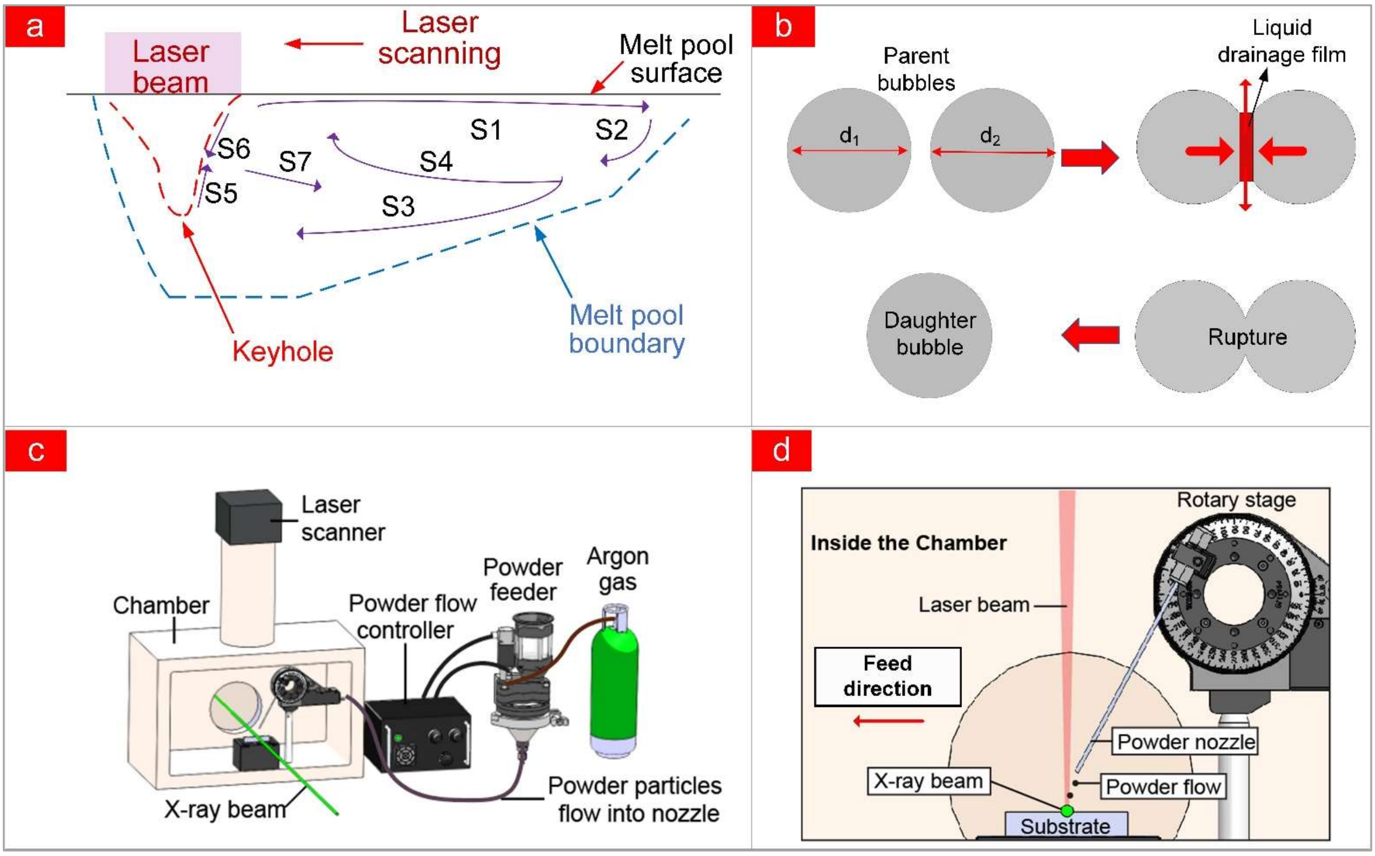

Fig. 1. (a) Schematic of the melt pool in L-DED and its different sections; (b) steps in the film drainage bubble coalescence model, starting with the collision of parent bubbles, then separated by a liquid drainage film, followed by their merge to a daughter bubble; (c) The in situ/operando experimental setup located at the 32-ID-B beamline at APS, consisting of a chamber with an inert environment, laser scanner, powder flow controller, powder feeder, and an argon gas cylinder. The L-DED process is probed by an X-ray beam that enters the chamber from a back viewport and is captured by a detector to generate real-time images; (d) a focused image of the system inside of the chamber showing a singular delivery nozzle mounted on a rotary stage to keep the delivery system aligned with the moving laser scanner, a substrate, and the laser beam.

Alloys) with equivalent spherical diameters ranging from 75 µm to 200 µm and an average of 88.2 µm was used. The scanning strategy for all the experiments was bidirectional where two layers with opposite scanning directions were printed on top of each other. The powder flow rate for all the experiments was 0.6 g/min with a deposition delay of 0.8 s. Powder was deposited with argon carrier gas onto a 50 mm long, 0.37 mm wide, and 2.84 mm tall Ti64 substrate.

Commercial L-DED systems typically have a melt pool in conduction mode. In conduction mode, the aspect of the keyhole (depth/width) is less than 0.5 [22]. The small aspect ratio of the vapor depression zone is a consequence of the attenuation of the laser beam by the high powder deposition rate. However, the energy density for the conducted experiments was specifically selected for keyhole melting mode with an aspect ratio greater than 0.5, which generated more vapor bubbles caused primarily by the fluctuation of the vapor depression zone [1, 12, 23]. Moreover, the characteristics of the HDH titanium feedstock can cause three types of bubble formation mechanisms [1]: (1) bubbles generated from the release of entrapped pores that already existed in the powder particles before being melted by the melt pool, (2) bubbles caused by the entrapment of gas from the top surface of the particles entrained into the melt pool, and (3) bubbles produced when gas is trapped under the bottom surface of the particles while they enter the melt pool [1]. Thus, the chosen input process parameters combined with the characteristic and shape of the irregular Ti64 powders may guarantee the formation of many bubbles in the melt pool.

The X-ray imaging detector system was composed of a high-speed camera Photron FastCam SA-Z, Japan), 10 × objective lens, a 45° reflection mirror, and a single crystalline scintillator of Lu3Al5O12: Ce with a 100 µm thickness [1, 14, 21]. The frame rate of the camera was set at 30,000 fps with a spatial resolution of 896 × 776 pixels, pixel size of 2 µm, and an exposure time of 5 µs [1, 14, 21]. An example of a captured X-ray image from Experiment 1 at time 25.3 ms is found in Fig. 2. It shows the different components and dynamics of the L-DED process in real-time, which include the tip of the singular nozzle system, the surface of the printed layer highlighted with a red dashed line, the deposition of the irregular Ti64 powder feedstock from the nozzle onto the melt pool, and the laser beam. In addition, the liquid-solid boundary of the melt pool is highlighted with a dashed yellow line, the large keyhole is indicated with a dashed red line, and the coalescence dynamic of the gas bubbles is also marked out inside a dashed yellow rectangle.

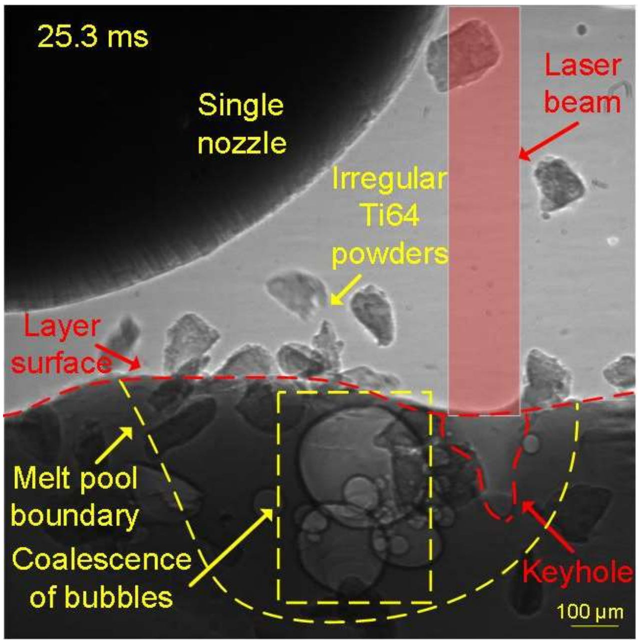

Fig. 2. X-ray image from Experiment 1 layer 2 at time 25.3 ms showing different components and dynamics in the L-DED process, such as the tip of the single nozzle, the deposition of the irregular HDH Ti64 powder feedstock, the laser beam, the melt pool boundary (in dashed blue), and the keyhole boundary (in dashed red), the top surface of the layer (in dashed yellow).

4. Data analysis methodology

Raw images from the X-ray imaging system were first processed to achieve a better contrast between different components in the process. Then, the analysis was divided into two parts. The first part investigated different types of forces that might have influenced the collision frequency between bubbles which was achieved by evaluating all the X-ray images to locate in which areas of the melt pool the bubbles are frequently moving prior to collision and drawing an assumption on which driving forces were the most dominant in those areas. The second part focused on analyzing the coalescence efficiency, using the film drainage model to measure contact time, which is possible with the high spatial and temporal resolution of the acquisition system. The high spatial resolution not only facilitated the measurement of the size of the bubbles in the order of microns, but also revealed the interaction and the deformation of the contact surfaces between the colliding bubbles, implying the formation of a thin liquid film. In addition, the contact time after a collision can also be determined in the order of µs, which rejects the theory of immediate coalescence proposed by the energy and critical approach velocity models.

Based on the film drainage model, three features were measured for each pair of colliding bubbles. In each set of measurements, d_1 represents the diameter of the larger bubble between the two bubbles, d_2 is the diameter of the smaller bubble, and $t_{contact}$ is the contact time between the two colliding bubbles. After collecting the measurements from Experiments 1 and 2, they were grouped into one data sample and were categorized as either coalescence or no coalescence of bubbles. As the analysis is a classification problem, a random forest model was applied to categorize the data and to determine which features are more significant to coalescence based on the mean decrease Gini index value. Usually, a low Gini index value indicates that a node in a decision tree contains large observations from the same class. With a high mean decreased Gini index value, a significant factor tends to split the data into groups that have more observations of the same classification [24]. The studied features included the bubble diameters, d_1, d_2, their ratio, d_1/d_2, their difference, d_1-d_2, the contact time $t_{contact}$, and the outcome was whether they coalesce or not. The random forest model works well for small to medium size data sets, such as the presented data in this investigation. The random forest models use bootstrapping sampling to create a larger data sample from the available sample and reduces the variance [24].

4.1. Image processing

The raw X-ray images were processed using the ImageJ software. For better contrast between different elements on the image, all the images were divided by the image that was captured before the laser was turned on and the powders were deposited from the nozzle. This procedure provided a better contrast between the three phases in the melt pool (gas, liquid and solid). Figure 3 shows the processed image equivalent to Fig. 2. The difference in contrast between the liquid and the solid phases is easily detected, and the melt pool boundary is traced using a yellow dashed line. Additionally, since the gas phase has a lower density compared to the densities of the liquid and solid phases, bubbles and the keyhole areas are easily identified in the melt pool X-ray images. Moreover, the top surface of the substrate (straight horizontal yellow dashed line) is clearly recognized from the deposited layer (red dashed line). However, some bright artifacts were observed in the processed images, due to in-flight particles in the “before” image. Nevertheless, these artifacts did not affect the analysis since they were fixed and easy to distinguish from other components in the images such as unmelted particles that had a darker contrast and were deposited either on the melt pool or on the solidified sections of the layer or caught on the glassy carbon plates.

4.2. Measurement of diameter

The diameters of the two bubbles during collision were measured using ImageJ. If the bubbles had a circular shape, the diameter was logged using the line tool in ImageJ. Otherwise, the effective diameter was calculated by tracing and measuring the area of the bubble and then using Eq. (3) where A represents the area of the traced irregular bubble and d_{eff} is the effective diameter.

$$d_{eff} = \sqrt{\frac{4 \times A}{\pi}} \tag{3}$$

Two examples of spherical and non-spherical bubbles, taken from Experiment 1, are displayed in Fig. 4a and b, respectively. The measurement of the diameter in Fig. 4a was done with the line tool, and in Fig. 4b, the area of the irregular shaped bubble was traced using the freehand selection tool in ImageJ to calculate the effective diameter. Moreover, the measurement unit in ImageJ was in pixels, and to convert from pixel to µm, the measured dimensions were multiplied by the spatial resolution 2 µm/pixel. Finally, the same method was also used to measure the diameter of a pore after solidification.

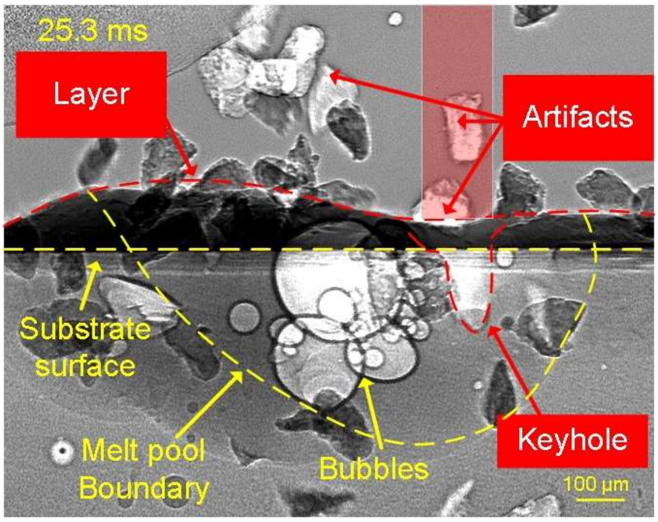

Fig. 3. Processed X-ray image from Experiment 1 at time 25.3 ms showing different components and dynamics in the L-DED process.

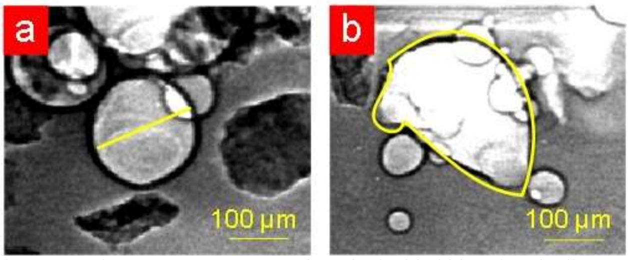

Fig. 4. (a) Diameter measurement of a spherical bubble using the line tool ImageJ; (b) tracing of a non-spherical bubble to measure the area and calculate the effective diameter.

4.3. Contact time and coalescence

As mentioned before, the contact time is the time where the two parent bubbles are in contact until they coalesce or separate. While the frame rate of the high-speed camera was set at 30,000 fps, the time difference between each X-ray frame is equal to 33 µs. The contact time can be measured using Eq. (4), where $t_{contact}$ (d_1, d_2) is the time of contact between two bubbles, d_1 and d_2 are the measured bubble diameters, N is the number of frames during which the two bubbles were in contact, and Δt is the time interval between two adjacent frames, which is 33 µs.

$$t_{contact}\left(d_1, d_2\right) = N \times \Delta t \quad (4)$$

For each case of collision, the diameters of the two bubbles were recorded and labeled as coalesced or not coalesced. Figure 5 displays a sequence of X-ray frames from Experiment 1 layer 2, where two bubbles b_1 and b_2 with respective diameters d_1 and d_2 of 144 µm and 115 µm, collided with each other and then coalesced. The sequence started at t_0, which depicted the time before the two bubbles collided and before b_2 moved towards b_1. At t_0 +33 µs, a thin film was created between the two deformed surfaces of the bubbles, which denotes the formation of a liquid film based on the film drainage model and indicates that the collision had occurred. At t_0 +198 µs, the two bubbles merged to form a new bubble, $b_{1,2}$. The number of frames in which the bubbles were in contact was 5, therefore $t_{contact}$ (144, 115) was equal to 165 µs. Figure 6 is another example of two bubbles that did not coalesce after colliding in Experiment 1 layer 2. In this sequence, t_0 represented the starting time where b_1 and b_2 collided, their respective diameters d_1 and d_2 were equal to 211 µm and 36.9 µm. From time t_0 to t_0 + 231 µs, the location of b_2 has changed due to the size fluctuations of b_1, which shows that the two bubbles stayed in contact for N=8 frames. The contact time, $t_{contact}$ (211, 36.9), was equal to 264 µs, until b_1 (the larger diameter bubble) pushed b_2 away at time t_0+297 µs in Fig. 6j, and the two bubbles were no longer in contact with each other.

5. Experimental results and discussion

The measurements and analysis of each layer summarized in Table 1, includes:

- The total number of bubbles created during printing in the entire process.
- The total number of collisions and coalescence that occurred between each pair of bubbles.
- The collision frequency, which was the ratio between the number of collisions over the total number of bubbles.
- The coalescence efficiency, which was the ratio between the number of coalescences over the number of collisions.
- The frequency of coalescence, which was the multiplication of the collision frequency and the coalescence efficiency.
- The diameter of the largest formed bubble in the melt pool before solidification for each layer.
- The diameter of the largest pore formed in the sample after solidification for each layer.

Table 1. Number of bubbles, collision and coalescence, and coalescence frequency

	Experiment 1		Experiment 2	
Layer	1	2	1	2
Total generated bubbles	76	279	123	620
Total collisions	18	206	56	663
Total coalescence	6	35	1	30
Collision frequency (%)	23.6	73.38	45.5	107
Coalescence efficiency (%)	33.3	16.9	1.78	4.52
Coalescence frequency (%)	7.8	12.5	0.81	4.83
Diameter of the largest bubble before solidification (*µm*)	113.8	331.4	199	312
Diameter of the largest pore after solidification (*µm*)	36.6	260	38.7	152.3

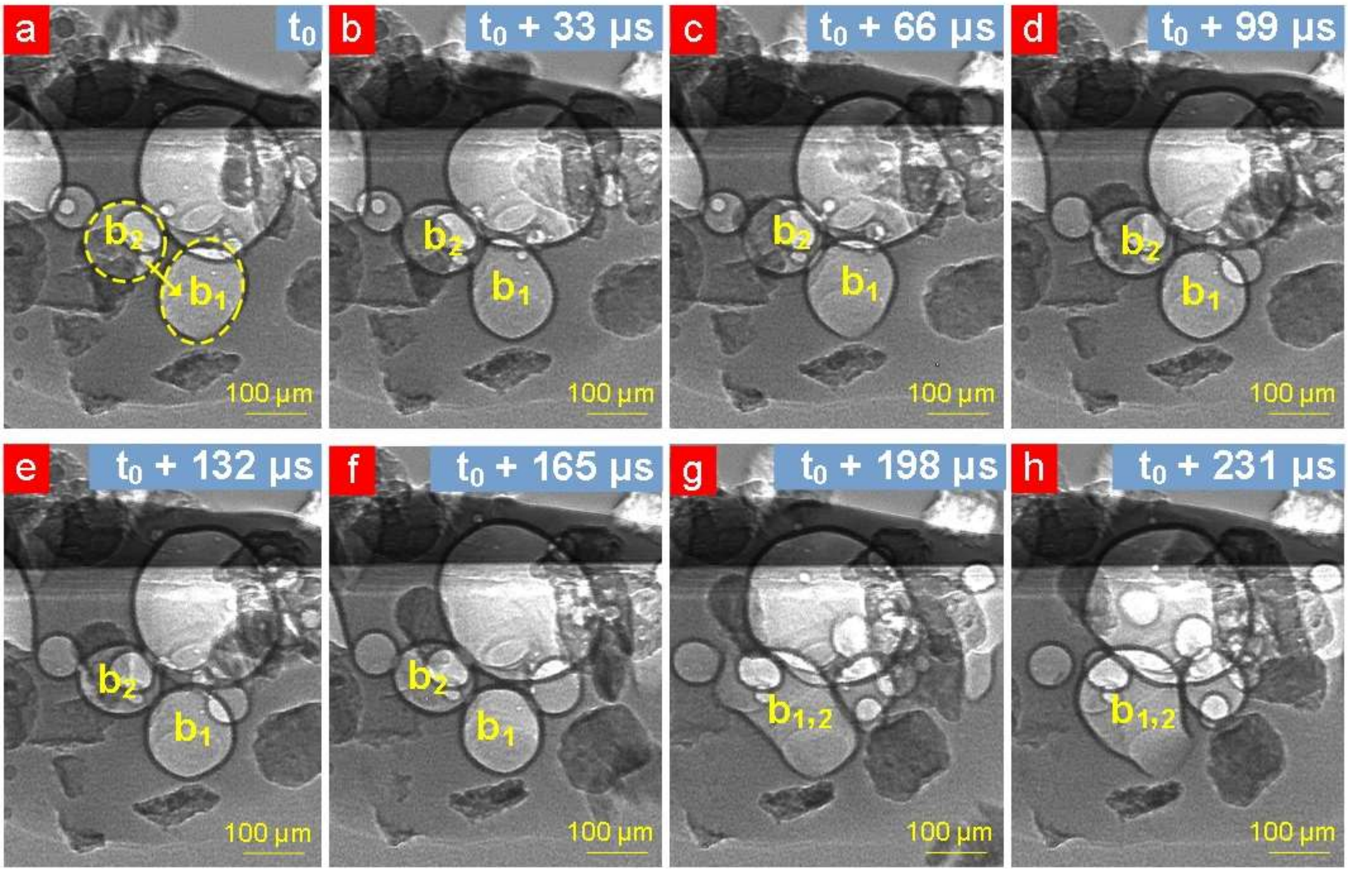

Fig. 5. Sequence of X-ray frames showing two parent bubbles coalescing during Experiment 1 layer 2, with t_0 as the time right before the two bubbles collided. The sequence starts at (a) t_0 and ends with (h) t_0 + 231 μs. The time of contact between the two bubbles (b_1 =144 μm and b_2 =115 μm) was 165 μs before merging and creating a new bubble $b_{1,2}$.

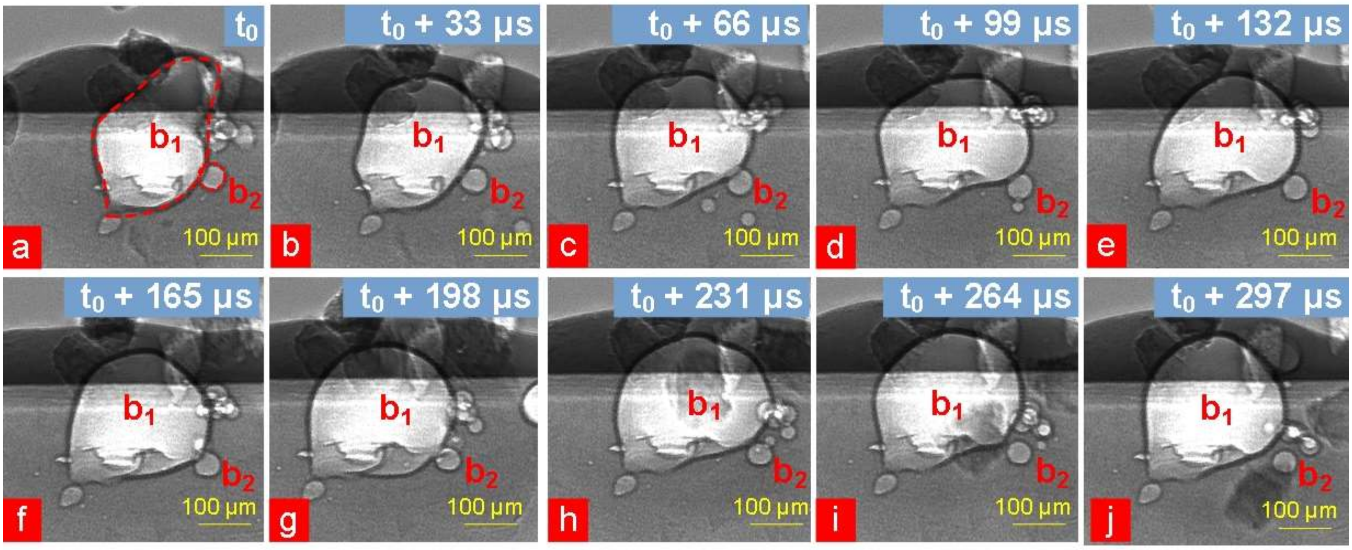

Fig. 6. Sequence of X-ray frames showing two parent bubbles colliding but not coalescing during Experiment 1 layer 2, with t_0 as the time when the two bubbles collided. The sequence starts at (a) t_0 and ends with (j) t_0 + 297 μs. The time of contact between the two bubbles (b_1 =211 μm and b_2 =36.9 μm) was 264 μs.

The measurements reveal that the number of created bubbles in the first layer is lower compared to the second layer for both experiments. This is due to the delay in the powder deposition system and its arbitrary behavior which might have been caused by clogging of powders in the nozzle, leading to fewer powders being deposited from the nozzle during the print of the first layer. This shows that two of the main factors of bubble formation include the powder characteristics and its interactions with the melt pool. Additionally, from the difference in the number of collisions between layers 1 and 2 for both experiments, the number of collisions increased with the number of bubbles generated, whereas in layer 2 of Experiment 2, the number of collisions exceeded the number of generated bubbles. On average for all layers, the collision frequency had an average of approximately 62%, but the coalescence efficiency was low with an average of 14%. Subsequently, the coalescence frequency had an overall low approximated average of 6.5%. The measured diameters of the largest formed bubble and formed pore for each layer in Table 1 show that a large quantity of generated bubbles in the melt pool led to producing large size bubbles and pores and this might affect the mechanical properties of the samples.

The major and key features that impacted the collision frequency and the coalescence efficiency, and therefore resulted in a low coalescence frequency, are described in the following section.

5.1. Collision frequency

The following section describes the instances in the experiments when collision did or did not occur and explains the major factors affecting the frequency of collision of gas bubbles in the liquid melt pool.

5.1.1. Non-collision

When there is a small number of bubbles generated during the process, the chance of two bubbles colliding is very low. As displayed in Table 1 for layer 1 in both experiments, the number of collisions was very low compared to the total number of generated bubbles. Most of the bubbles that did not collide formed near the bottom tip of the keyhole or near the center of the keyhole on the trailing edge side of the melt pool, in areas similar to sections S5 and S7 from Fig. 1a., where the possible dominant forces were the Marangoni flow, the vaporization pressure and the acoustic waves. In general, Marangoni flow directed the flow of the melt pool from a region of lower surface tension to a region of higher surface tension [4]. Moreover, the behavior of the surface tension is inversely proportional to the temperature and directly proportional to the presence and movement of elements located in the melt pool [4]. Therefore, areas with higher temperatures such as S5 had a lower surface tension, as opposed to areas deeper in the melt pool where the temperatures were lower; hence they had a larger surface tension. Also, when more elements (e.g., bubbles) appear in a specific area in the melt pool, their overall area will decrease the surface tension of the liquid in that location. However, because there were few bubbles present in the center of the melt pool, there was no effect on the surface tension in that location.

As for the vaporization pressure, a pressure force from the vapor depression zone propelled the liquid flow along with the bubbles away from the keyhole [25]. Acoustic waves from keyhole tip fluctuation drove bubbles to the center of the melt pool. Furthermore, bubbles were also driven upwards to the surface of the melt pool; one possible explanation was the presence of a buoyancy force, which is proportional to the thermal gradient [21]. Areas near the keyhole and the liquid-solid boundary exhibit a large thermal gradient due to the large temperature difference between the existing different phases. Therefore, a buoyancy force was exerted on the bubbles in those areas moving the bubble away from the bottom of the melt pool or near the keyhole area to the surface of the melt pool. To conclude, a combination of the Marangoni flow, vaporization pressure, acoustic waves and buoyancy force were most likely the dominant forces in bubble trajectories that prevent collision, driving the bubbles to move backward and upward and allowing the bubble to escape through the top surface.

Figure 7 is an X-ray sequence displaying a bubble behind the keyhole near its center, which was driven to the surface after formation in layer 1 of Experiment 2. At time t_0, the keyhole did not fluctuate, and no bubbles formed. At t_0 + 33 μs, one bubble, b_1, formed due to the fluctuation of the keyhole at its center. This bubble was then pushed by a combination of acoustic waves and the Marangoni flow towards the back of the melt pool, and then upward to the surface by the buoyancy force. Bubble b_1 did not collide with any other bubble in the melt pool and at t_0 + 99 μs, b_1 reached the top surface of the melt pool. The yellow arrows in Fig. 7c and d indicate the trajectory of bubble b_1. Figure 8 is a schematic of the melt pool in the L-DED process, describing the different forces and trajectories of the bubbles in sections S5 and S7 of the melt pool when no collision occurred.

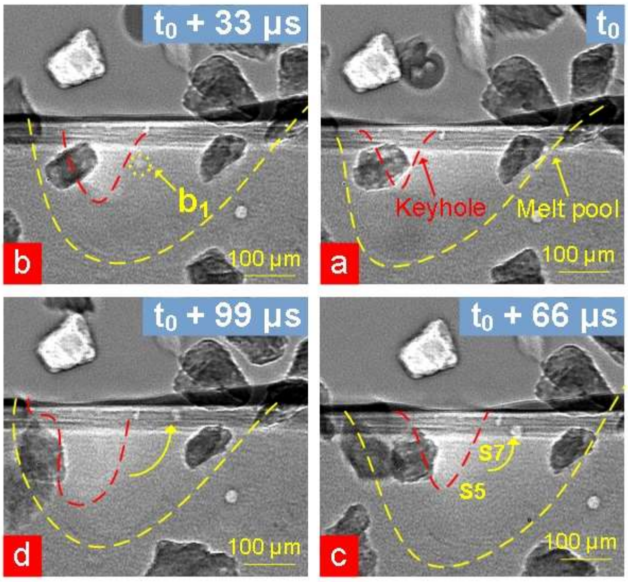

Fig. 7. Sequence of X-ray frames from layer 1 in Experiment 2 with scanning direction of the laser from right to left. t_0 was the time right before bubble b_1 was formed. b_1 did not collide with any other bubble and was forced to the top surface by the combination of the Marangoni flow, acoustic waves, and the buoyancy force in sections S5 and S7.

5.1.2. Collision

With the increase of formed bubbles in the melt pool, collisions were more frequent. Most new bubbles were created on the surface of the melt pool near the keyhole. They were introduced to the melt pool either in the area behind the keyhole (red dashed rectangle in Fig. 9a) or in front of the keyhole (yellow dashed rectangle in Fig 9.a). Both areas can be referred to as section S6 of the melt pool from Fig.1a,

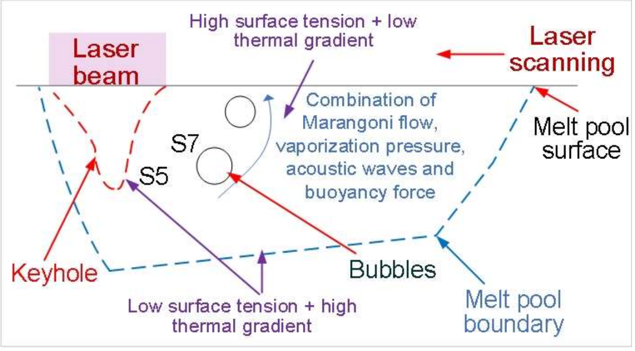

Fig. 8. A schematic showing the pattern of the bubbles due to the combination of the Marangoni flow, the acoustic waves and buoyancy force and no collision in sections S5 and S7

where the Marangoni flow and the vaporization pressure drove the newly created bubbles to move downwards and to the center of the melt pool. In addition, these forces were occasionally coupled by acoustic waves from the fluctuated tip of the depression zone, which pushed the bubbles into the center of the melt pool, similar to the section S7 in Fig. 1a. Other bubbles in section S1, were driven to the back of the melt pool by Marangoni flow.

Bubbles in the melt pool can be divided into two types, stationary and nonstationary. The nonstationary bubbles either collide with each other while moving in the melt pool due to the forces in the flow, or they collide with stationary bubbles. These stationary bubbles were fixed in the melt pool due to two possible cases: (1) they were pinned at the liquid-solid boundary after being pushed by the forces mentioned previously or (2) they were large enough to overcome the buoyancy force. Furthermore, Leung *et al.* indicated that the oxide layer on the surface of the bubbles was another reason that caused the bubbles to stabilize in an L-PBF process using an Invar 36 powder bed [20]. In this study, investigations were not conducted to show evidence of the existence of an oxide layer on the bubbles but will be performed as future work to confirm the presence of the oxide layers on the bubbles generated from the irregular HDH Ti64 powders. Larger stationary bubbles acted as a target for other bubbles to collide with and were divided into three types: (1) large bubbles generated from the characteristics of particles and their interaction with the melt pool; (2) large bubbles caused by the coalescence of bubbles into one large bubble; (3) bubbles which expanded with time inside the melt pool due to the increase of gas temperature and the reduction of interfacial energy after stabilization in the melt pool [20]. After the collision, each bubble stayed in contact for an interval of time until they either separated or coalesced.

Figure 9 is a sequence of X-ray images covering collision mechanisms that occurred in layer 2 of Experiment 2 by showing the dynamics of two bubbles b_1 and b_2. In Fig. 9a, t_0 represented the time when b_2 formed. Figure. 9b shows how the lower part of b_1 pinned to the liquid-solid boundary of the melt pool. With time, b_1 increased in size as it is shown in Fig. 9b, c, and d, and due to its large size, more bubbles collided with b_1. Simultaneously, b_2 was a bubble introduced

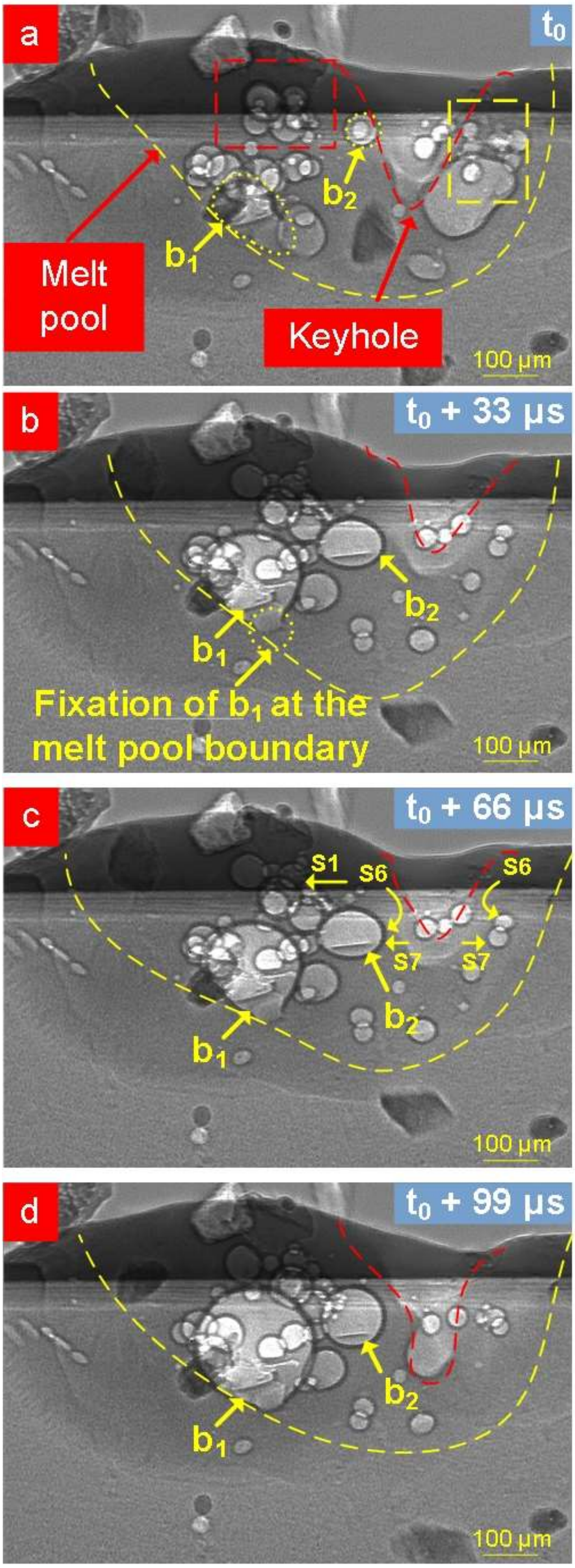

Fig. 9. Sequence of X-ray frames from layer 2 of Experiment 2 showing bubble dynamics when the number of bubbles and the frequency of collision are high. The scanning direction of the laser was from left to right. t_0 is the time when b_2 was formed at the top surface in the area behind the keyhole. The dominant forces were the Marangoni flow, the vaporization pressure, and the acoustic wave. In addition, it reveals how two bubbles b_1 and b_2 increase in size with time in sections S1, S6 and S7.

to the melt pool near the keyhole at t_0 and had a relatively large size. Then bubble b_2 moved downward by the dominant forces in that area, which were the Marangoni flow and the vaporization pressure (S6). The diameter b_2 increased in size as shown in Fig. 9b, -d, which allowed this bubble to overcome the buoyancy force and not move upward toward the surface. In Fig. 9b and c, the acoustic waves from keyhole fluctuation pushed b_2 to the center of the melt pool behind the keyhole (S7). The trajectory of b_2 is indicated by yellow arrows in Fig. 9c. Furthermore, a dashed yellow box in Fig. 9a, shows that bubbles were also formed in front of the keyhole and had a similar trajectory pattern (indicated by yellow arrows in Fig. 9c) as the bubbles created behind the keyhole. Moreover, bubbles in the top surface of the melt pool, which are highlighted by the red dashed box in Fig. 9a, are subject to the Marangoni flow and are driven towards the back while colliding with each other (S1). These bubbles' movement is marked by a yellow horizontal arrow near the substrate's top surface in Fig. 9c. Lastly, Fig. 10 is a schematic representation of all the bubble dynamics in the melt pool which favored collision in sections S1, S6 and S7 of the melt pool. After coalescing, some daughter bubbles increased in size and either exploded or remained after solidification, resulting in a large pore in the sample. Though this study did not focus on the dynamics of the daughter bubbles, future study should underline these phenomena and how they can affect the mechanical properties of the final build.

Finally, some of the bubbles were in areas S2, S3 and S4 in reference to Fig. 1a. However, these bubbles were not affected by the forces that governed those areas. One probable reason was that bubbles became stationary in the center or the back of the melt pool and collided with other bubbles. Another likely reason was because the movement of the bubbles from the back towards the area near the keyhole, was restricted by the large density of colliding bubbles.

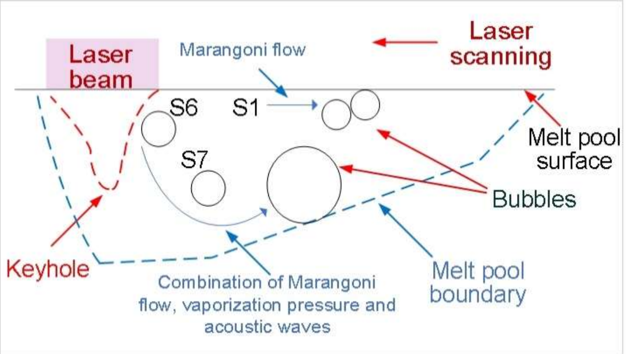

Fig. 10. A schematic showing the pattern of the bubbles due to the Marangoni flow, the vaporization pressure, and the acoustic waves and when collision occurred in sections S1, S6 and S7.

5.2. Coalescence efficiency

For each pair of colliding bubbles, the following data was collected: the measured d_1 (the larger diameter in µm) and d_2 (the smaller diameter in µm), $t_{contact}$ (ms), the calculated ratio d_1/d_2, and the difference d_1-d_2. This data was grouped into two categories (either they coalesced, or they did not coalesce), and the random forest model was applied (using R programming language) to the sample that included 943 colliding instances in total from Experiments 1 and 2 combined. The confusion matrix in Table 2 was constructed by the random forest model using a random sample of 2 factors. The values 858 and 22 represent the number of observations that were respectively classified correctly as No coalescence and Yes coalescence by the random forest model, and the values 13 and 50 are the number of observations that were classified incorrectly by the model. The accuracy of the model was calculated at 93%, however by looking only at the Yes coalescence group, 70% of the coalescences were predicted wrong. As the study's focus is the efficiency of coalescence in the data, the accuracy of predicting only the coalescence was not the main objective. To precisely predict if coalescence occurred, other machine learning models should be applied in the future. The importance chart based on the mean decrease Gini index value was also generated in Fig. 11, and it reveals that the diameter of the smallest bubble, d_2, is the most significant factor and the time of contact is the least significant.

Table 2. Confusion matrix of the random forest model

	Predicted No	Predicted Yes
Actual No	858	13
Actual Yes	50	22

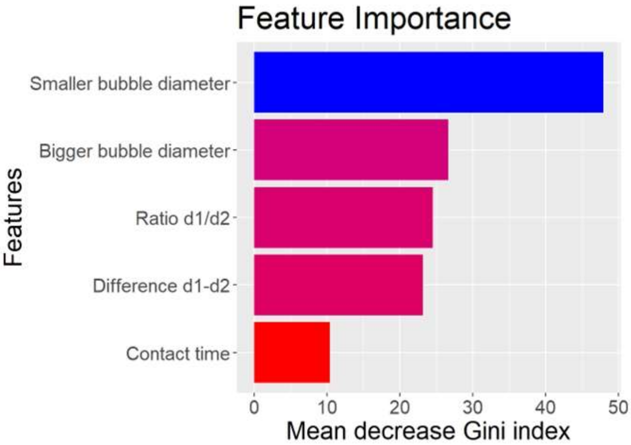

Fig. 11. Importance chart based on the mean decrease Gini index value from the random forest model.

Figure 12 displays four scatter plots, plotted in each the smaller diameter d_2 against the other four features. It is apparent from all the plots that the data points can separated into two regions by a horizontal line at a constant d_2 value, where above this line the coalescence is visible to detect. To find a common threshold for all the plots, one decision tree using a simple classification tree model was constructed using R software to see the first split condition. The first split was done at d_2 =76 µm, so that when the diameter of the smaller bubble was less than 76 µm, the coalesce efficiency $\lambda (d_1, d_2)$ was equal to 3.5%. And when the smaller diameter was bigger than 76 µm, $\lambda (d_1, d_2)$ was around 48%. This shows that the coalescence efficiency was higher when the smaller diameter is larger than 76 µm.

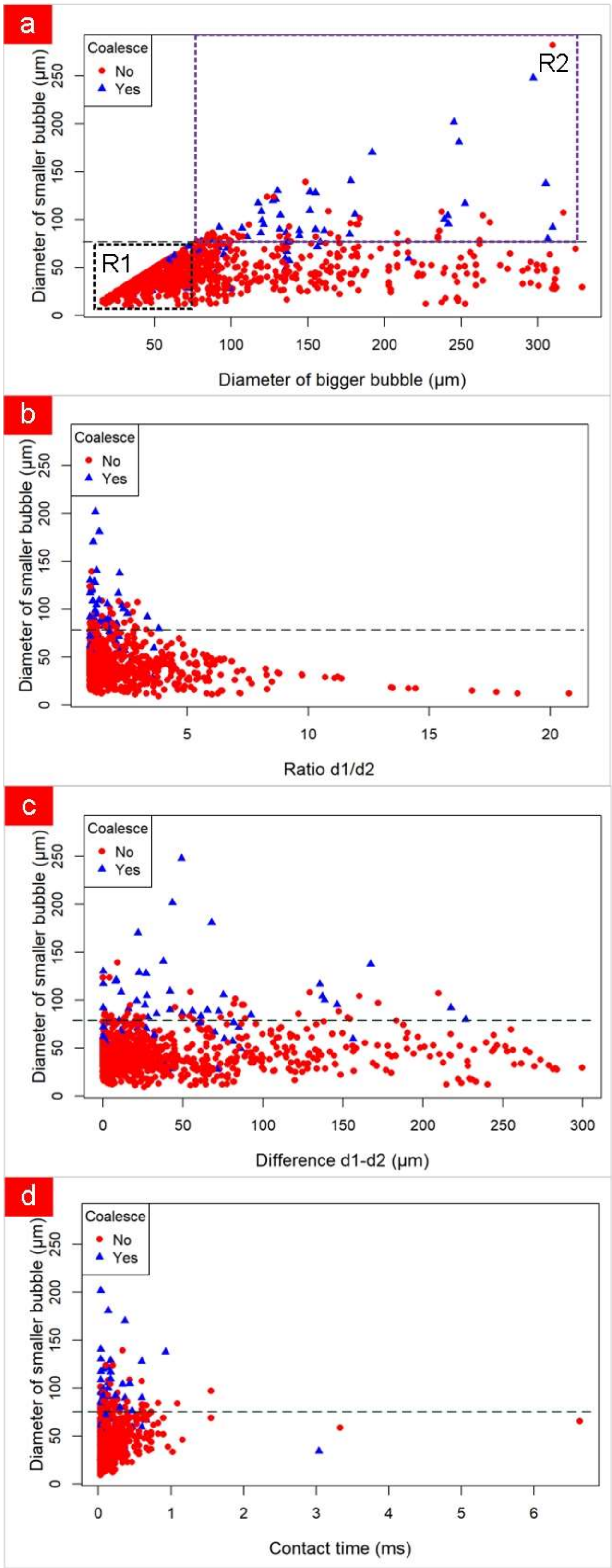

Fig. 12. Scatterplots showing the smaller diameter d_2 against all four other features.

Figure 12a, displays a large density of collision points between bubbles that had d_1 and d_2 both smaller than 76 µm (section R1 inside the black dashed rectangle), but with low coalescence efficiency. Figure 12a also shows a smaller density of pairs of bubbles where both of their diameters were larger than 76 µm and exhibits higher coalesce efficiency (section R2 inside the purple dashed rectangle). This shows that the use of irregular HDH Ti64 powder feedstock in L-DED produced a large quantity of small bubbles that had a high percentage of colliding, but their merging efficiency was low, and only bubbles where the smaller diameter of the pair was larger than the threshold of 76 µm had a higher efficiency of merging. Furthermore, from Fig. 12b, it can be noted that most of the coalescing instances had a ratio (d_1/d_2) approaching 1 and that from Fig .12c, the larger difference (d_1-d_2) between the two coalescing bubbles was around 225 µm.

6. Conclusion

Two experiments were conducted for a L-DED process with irregular HDH Ti64 powder feedstock onto a Ti64 substrate. The experiments were monitored using a high-speed X-ray imaging system to investigate the bubble coalescence mechanism during the process. The bubbles coalescence frequency depends on the frequency of collision and the coalescence efficiency.

By observing the X-ray images, the number of bubbles generated in the melt pool was small, the frequency of collision was low and the movement of the bubbles in the melt pool toward the top surface was governed by the Marangoni flow, the acoustic waves, and the vaporization pressure combined with the buoyancy force. When the number of bubbles was larger, the numbers of collisions were higher, and the bubbles were driven inside the melt pool to the center or back by the following forces:

- The Marangoni flow, the vaporization pressure, and the acoustic waves from the fluctuation of the tip of the keyhole, when the bubbles were close to the vaporization zone.
- The Marangoni flow when the bubbles were at the top surface of the melt pool.

The results also showed collisions between two non-stationary bubbles and collisions between non-stationary bubbles and stationary bubbles. Stable bubbles were usually fixed in the melt pool due to their large size overcoming the buoyancy force or were pinned at the liquid-solid boundary of the melt pool. When the non-stationary bubbles became stable, their size started to increase due to the lower interfacial energy and turned into a target for more bubbles to collide with.

The coalescence efficiency analysis was based on the film drainage model, where the efficiency depended on the diameters of the two colliding bubbles and the contact time before merging or separating. The efficiency of coalescence was reported to be low with an average of 14% for all experiments. A threshold for the smaller diameter bubble was generated and was found to be equal to 76 µm. The coalescence efficiency was 3.5% below the threshold diameter and 48% above the threshold. Results showed that irregular HDH Ti64 powders often produced a large quantity of small gas bubbles in the melt pool which collided at a high rate but had a low coalescence efficiency.

Future investigations should focus on checking the presence of an oxide film layer on bubbles created from irregular HDH Ti64 powder feedstock that can affect the movement in the bubbles in the melt pool and the coalescence frequency. Furthermore, future studies should be conducted on the dynamics of the daughter bubbles after coalescing and examine how they can affect the percentage of porosity and the mechanical properties of the final build. Moreover, the correlation between varying input parameters, close to L-DED real application input parameters, and the coalescence mechanism should be considered and analyzed. In addition, further statistical analysis can investigate the importance of the keyhole and melt pool features as well as process parameters to bubbles coalescence. Moreover, other machine learning models can be tested and implemented to predict the coalescence frequency in future experiments. Finally, future work includes finding the relationships between large bubble coalescence and thermal history to predict and mitigate porosity.

Acknowledgements

The authors would like to thank Tao Sun, Niranjan Parab, Kamel Fezzaa, and Alex Deriy at the beamline. This research used resources of the Advanced Photon Source, a U.S. Department of Energy (DOE) Office of Science User Facility operated for the DOE Office of Science by Argonne National Laboratory (ANL) under Contract No. DE-AC02-06CH11357 and support through Laboratory Directed Research and Development (LDRD) funding from ANL under the same contract.

References

[1] Wolff SJ, Wang H, Gould B, Parab N, Wu Z, Zhao C, Greco A, Sun T. In Situ X-Ray Imaging of Pore Formation Mechanisms and Dynamics in Laser Powder-Blown Directed Energy Deposition Additive Manufacturing. International Journal of Machine Tools and Manufacture 2021; 166: 103743.

[2] Saboori A, Aversa A, Marchese G, Biamino S, Lombardi M, Fino P. Application of Directed Energy Deposition-Based Additive Manufacturing in Repair. Applied Sciences 2019; 9(16): 3316.

[3] Razavi S, Bordonaro G, Ferro P, Torgersen J, Berto F. Fatigue Behavior of Porous Ti-6Al-4V Made by Laser-Engineered Net Shaping. Materials 2018; 11(2): 284.

[4] Zhang P, Zhou X, Cheng X, Sun H, Ma H, Li Y. Elucidation of Bubble Evolution and Defect Formation in Directed Energy Deposition Based on Direct Observation. Additive Manufacturing 2020; 32: 101026.

[5] Wilson JM, Piya C, Shin YC, Zhao F, Ramani K. Remanufacturing of Turbine Blades by Laser Direct Deposition with Its Energy and Environmental Impact Analysis. Journal of Cleaner Production 2014; 80, p. 170–178.

[6] Bennett J, Garcia D, Kendrick M, Hartman T, Hyatt G, Ehmann K, You F, Cao J. Repairing Automotive Dies With Directed Energy Deposition: Industrial Application and Life Cycle Analysis. Journal of Manufacturing Science and Engineering 2019; 141(2): 021019.

[7] Chen Y, Clark SJ, Huang Y, Sinclair L, Lun Alex Leung C, Marussi S, Connolley T, Magdysyuk OV, Atwood RC, Baxter GJ, Jones MA, Todd I, Lee PD. In Situ X-Ray Quantification of Melt Pool Behaviour during Directed Energy Deposition Additive Manufacturing of Stainless Steel. Materials Letters 2021; 286: 129205.

[8] Razavi S, Bordonaro G, Ferro P, Torgersen J, Berto F. Fatigue Behavior of Porous Ti-6Al-4V Made by Laser-Engineered Net Shaping. Materials 2018; 11(2): 284.

[9] Kouraytem N, Chiang PJ, Jiang R, Kantzos C, Pauza J, Cunningham R, Wu Z, Tang G, Parab N, Zhao C, Fezzaa K, Sun T, Rollett AD. Solidification Crack Propagation and Morphology Dependence on Processing Parameters in AA6061 from Ultra-High-Speed x-Ray Visualization. Additive Manufacturing 2021; 42: 101959.

[10]Yu W, Sing SL, Chua CK, Tian. Influence of Re-Melting on Surface Roughness and Porosity of AlSi10Mg Parts Fabricated by Selective Laser Melting. Journal of Alloys and Compounds 2019; 792, p. 574–581.

[11]Chen Z, Han C, Gao M, Kandukuri SY, Zhou K. A Review on Qualification and Certification for Metal Additive Manufacturing. Virtual and Physical Prototyping 2022; 17(2), p. 382–405.

[12]Zhao C, Parab ND, Li X, Fezzaa K, Tan W, Rollett AD, Sun T. Critical Instability at Moving Keyhole Tip Generates Porosity in Laser Melting. Science 2020; 370(6520), p. 1080–1086.

[13]Chen Y, Clark SJ, Sinclair L, Leung CLA, Marussi S, Connolley T, Magdysyuk OV, Atwood RC, Baxter GJ, Jones MA, McCartney DG, Todd I, Lee PD. In Situ and Operando X-Ray Imaging of Directed Energy Deposition Additive Manufacturing. 2020.

[14]Wang H, Pfefferkorn FE, Wolff SJ. Investigation of Pore Formation Mechanisms Induced by Spherical-Powder Delivery in Directed Energy Deposition Using in Situ High-Speed X-Ray Imaging. Additive Manufacturing Letters 2022; 3: 100050.

[15]Narra SP, Wu Z, Patel R, Capone J, Paliwal M, Beuth J, Rollett A. Use of Non-Spherical Hydride-Dehydride (HDH) Powder in Powder Bed Fusion Additive Manufacturing. Additive Manufacturing 2020; 34: 101188.

[16]Terrassa KL, Haley JC, MacDonald BE, Schoenung JM. Reuse of Powder Feedstock for Directed Energy Deposition. Powder Technology 2018; 338, p. 819–829.

[17]Xu W, Xiao S, Lu X, Chen G, Liu C, Qu X. Fabrication of Commercial Pure Ti by Selective Laser Melting Using Hydride-Dehydride Titanium Powders Treated by Ball Milling. Journal of Materials Science & Technology 2019; 35(2), p. 322–327.

[18]Liao Y, Lucas D. A Literature Review on Mechanisms and Models for the Coalescence Process of Fluid Particles. Chemical Engineering Science 2010: 65(10): 2851–2864.

[19]Leung CLA, Marussi S, Atwood RC, Towrie M, Withers PJ, Lee PD. In Situ X-Ray Imaging of Defect and Molten Pool Dynamics in Laser. Additive Manufacturing 2018; Nat Commun, 9(1): 1355.

[20]Leung CLA, Marussi S, Towrie M, Atwood RC, Withers PJ, Lee PD. The Effect of Powder Oxidation on Defect Formation in Laser Additive Manufacturing. Acta Materialia 2019; 166, p. 294–305.

[21]Wang H, Gould B, Haddad M, Moorehead M, Couet A,Wolff SJ. In Situ High-Speed Synchrotron X-Ray Imaging of Laser-Based Directed Energy Deposition of the Alloying Process with Dissimilar Powders. Journal of Manufacturing Processes 2022; 75, p. 1003–1011.

[22]Hojjatzadeh SMH, Parab ND, Guo Q, Qu M, Xiong L, Zhao C, Escano LI, Fezzaa K, Everhart W, Sun T, Chen L. Direct Observation of Pore Formation Mechanisms during LPBF Additive Manufacturing Process and High Energy Density Laser Welding. International Journal of Machine Tools and Manufacture 2020; 153: 103555.

[23]Zhao C, Fezzaa K, Cunningham RW, Wen H, De Carlo F, Chen L, Rollett AD, Sun T. Real-Time Monitoring of Laser Powder Bed Fusion Process Using High-Speed X-Ray Imaging and Diffraction. Sci Rep 2017; 7(1): 3602.

[24]James G, Witten D, Hastie T, Tibshirani R. An introduction to statistical learning: With applications in R 2017; Springer.

[25]Eriksson I, Powell J, Kaplan AFH. Melt Behavior on the Keyhole Front during High Speed Laser Welding. Optics and Lasers in Engineering 2013; 51(6), p. 735–740.